Proceedings of The Thirteenth (2003) International Offshore and Polar Engineering Conference
Honolulu, Hawaii, USA, May 25−30, 2003

ISBN 1−880653-60−5 (Set); ISSN 1098−6189 (Set)

Wave Interaction with a Sea Dike Using a VOF Finite-Volume Method

Peter Troch[1] *Tingqiu Li*[1] *Julien De Rouck*[1] *David Ingram*[2]

[1] Department of Civil Engineering, Ghent Universit
Zwijnaarde, Belgium
[2] Center for Mathematical Modelling and Flow Analysis,
Manchester Metropolitan University
Mancheste, UK

ABSTRACT

This paper represents a solver for numerical simulation of breaking waves, developed at Ghent University using an implicit cell-staggered VOF finite volume approach. The mathematical model is based on unsteady incompressible Navier-Stokes (NS) equations with a free surface. A flux-difference splitting approach with the MUSCL type (or the ENO scheme) and a central-difference scheme are applied for evaluation of the inviscid and viscous fluxes, respectively. A projection method is involved for coupling of the pressure and the velocity. A free surface is tracked with the VOF method, in which the approximate dynamic boundary conditions are implemented. In addition, second- and fourth-order artificial damping terms are introduced to the velocity normal to the cell face. A Sommerfeld radiation condition is implemented at the open boundary to dissipate the energy of outgoing waves. Moreover, cut-cell techniques are utilized for treatment of an arbitary geometry. The solver can capture many physical phenomena during the interaction of waves with a dike, when a wave run-up and overtopping over an impermeable sea dike are performed in a numerical wave tank.

KEY WORDS: Breaking waves, wave-structure interaction in a viscous flow, an implicit cell-staggered VOF finite volume solver, and a cut-cell Cartesian mesh.

INTRODUCTION

Just recent years, the primary emphasis in the coastal engineering is on the detection of the fine scale feature of the complex flow fields for the coastlines, especially under the circumstances of beraking waves. An elucidation of such detailed mechanisms is always desirable in the region of interest. The capability of a numerical scheme that incorporates the treatment of topological change of the interface provides one possibility for this purpose using the advanced CFD techniques. This is one of the main interests of industry and the results could be directly applied for performance analysis and design of dikes.

A sea dike encounters complex phenomena like wind-generated breaking wave problems under a certain wind level. This is associated with vortex formation, turbulence and the behavior of moving air-water interface referred as a free surface. Since the free surface is determined as part of the solution (only its initial location and geometry are known in advance), topological changes related to the processes of merging and breaking, including a turbulence, amplify such a problem. A powerful numerical tool is preferred for treatment of arbitraily shaped interface in a natural way. The volume-of-fluid (VOF) method is one of the most popular schemes for studying flows of immiscible fluids with interfaces. The characteristic is that it is not necessary to renew the mesh, which ensures that the computations can be performed on a fixed grid. The mass conservation is its intrinsic feature. Additionally, it does not require special procedures to model topological changes of the front. In the VOF method, the data structure that represents the interface is the volume fraction α of each surface cell that satisfies $0 < \alpha < 1$. Just the data α are specified at the beginning of a computational cycle according to the known shape and location of an interface.

To evaluate the volumetric fluxes of α crossing a certain face, it is necessary to provide the geometrical information from the reconstructed interface. Typically, this is classified as two basic categories: the Eulerian and Lagrangian interface reconstruction. For the Eulerian interface reconstruction, one tracks the volume in cells that contain the interface rather than the interface itself. Therefore, this method is implicit without explicit interface re-

construction (e.g., Hirt and Nichols, 1981) or an interface to be determined according to the values of α (e.g., Youngs, 1982). These two types of the reconstruction are widely applied. One is to introduce a piecewise-constant or staircase representation of the interface, which sometimes is called as the original Hirt and Nichols's VOF method. This type is also referred as the SLIC (simple line interface calculation) algorithm. It allows that interfaces are arbitrarily orientated with respect to the computational grid. Alternative is to apply various PLIC (piecewise linear interface calculation) methods. This is more exact approximation to the interfaces once various possible orientations of the interface are predefined well. It can give much better results than the original VOF method (Rider and Kothe, 1998). For Lagrangian interface reconstruction, the PLIC-type interfaces can be moved in Lagrangian sense. As a result, it is explicit, that is, an interface is given with a local velocity at a certain cell face. The stretching or compression of the interface can be taken into account during each single fractional step. Moreover, the front does not diffuse. This approach is more robust as compared with the Eulerian reconstruction algorithm (Gueyffier et al., 1999).

On the other hand, one has to resolve the following transport equation for α

$$\frac{\partial \alpha}{\partial t} + \frac{\partial (u\alpha)}{\partial x} + \frac{\partial (v\alpha)}{\partial y} + \frac{\partial (w\alpha)}{\partial z} = 0 \qquad (1)$$

provided that the velocity field and the reconstructed interface are given. Since α is scalar quantity carrying the material information, this updates the values of α in each surface cell but maintains $\alpha = 1$ in the water and $\alpha = 0$ in the air. Numerical accuracy of resolution of Eq. (1) depends on the capture of a shape of a free surface and its location together with a suitable numerical approach.

In this paper, we developed a new solver for modelling of the breaking waves. The NS equations are resolved using cell-staggered finite volume (FV) on a cut-cell Cartesian mesh and a split-implicit time differencing scheme, while incompressibility is enforced through an iterative Poisson solver for the pressure. A free surface is tracked with the original VOF approach due to its simplicity (only solution of Eq. 1). In particular, it generalizes well to three dimensions (3D) and for several industrial application as well. Unfortunately, with this VOF method, the small error like the flotsam generated by advancing interface needs to be eliminated (Lafaurie et al., 1994), and it does not preserve local boundedness (Ubbink and Issa, 1999). The former may lead to error accumulation, and the latter can create an unphysical volume fraction. Therefore, our work in this area is to develop an approach which preserves both the smoothness of the interface and its sharp definition over one cell. The critical issue in this type of method is to discretize the convective term. This requires that numerical diffusion related with an upwind scheme should not be excessive, that is, without dispersing or wrinkling. The scheme includes an operator split advection algorithm, a blend of Hirt-Nichols's reconstruction algorithm and Ubbink and Issa's high resolution method, and a second-order explicit Adams-Bashforth scheme for achievement of a second-order accuracy in time. Our computation shows that it is simple and computationally efficient.

This paper is organized as follows. Firstly, we briefly describe numerical methods, which include the mathematical model, an implicit cell-staggered FV approach over a cut cell and the initial and boundary conditions. The calculated results, such as the convergence properties, the study of grid effects and the wavy flow fields, are presented next, followed by the concluding remarks.

NUMERICAL METHODS

Numerical method is to apply an implicit cell-staggered VOF finite volume approach for solution of the NS equations with a free surface. The interaction between the pressure and the velocity is realized with a projected algorithm. A cut-cell technology is implemented in order to deal with an arbitary geometry. The description in more detail will be found in Li et al., (2003).

Mathematical Model

Mathematical model is based on three-dimensional unsteady incompressible Navier-Stokes equations on a Cartesian cut-cell grid. A right-handed coordinate system (x, y, z, t) is set up (see

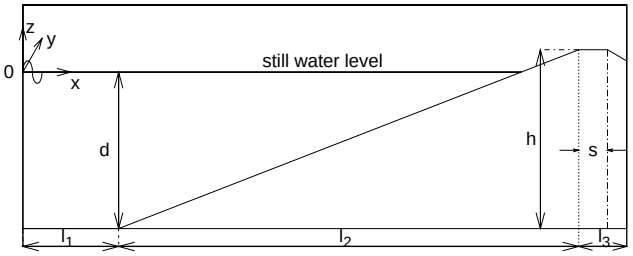

Figure 1: A reference coordinate system for seadike problems.

Fig. 1). The original is fixed at the intersection of the inlet with the still water level, x is positive along the direction of wave propagation, y is positive towards the width of a dike and z is positive upwards. Within this framework, the NS equations in a conservative form may be expressed as follows:

$$\frac{\partial \varphi}{\partial t} + \frac{\partial F}{\partial x} + \frac{\partial G}{\partial y} + \frac{\partial H}{\partial z} = Q \qquad (2)$$

where the variables $\varphi = (0,\ u,\ v\ , w)^T$ and $F = F_i - F_v + F_a,\ G = G_i - G_v + G_a,\ H = H_i - H_v + H_a$. The inviscid fluxes $(F_i,\ G_i,\ H_i)$, the viscous fluxes $(F_v,\ G_v,\ H_v)$, the acoustic fluxes $(F_a,\ G_a,\ H_a)$ and the source term (Q) are respectively

$$F_i = \begin{pmatrix} 0 \\ u^2 \\ vu \\ wu \end{pmatrix},\ G_i = \begin{pmatrix} 0 \\ uv \\ v^2 \\ wv \end{pmatrix},\ H_i = \begin{pmatrix} 0 \\ uw \\ vw \\ w^2 \end{pmatrix}. \qquad (3)$$

$$F_v = \begin{pmatrix} 0 \\ \nu_e \frac{\partial u}{\partial x} \\ \nu_e \frac{\partial v}{\partial x} \\ \nu_e \frac{\partial w}{\partial x} \end{pmatrix},\ G_v = \begin{pmatrix} 0 \\ \nu_e \frac{\partial u}{\partial y} \\ \nu_e \frac{\partial v}{\partial y} \\ \nu_e \frac{\partial w}{\partial y} \end{pmatrix},\ H_v = \begin{pmatrix} 0 \\ \nu_e \frac{\partial u}{\partial z} \\ \nu_e \frac{\partial v}{\partial z} \\ \nu_e \frac{\partial w}{\partial z} \end{pmatrix}. \qquad (4)$$

$$F_a = \begin{pmatrix} u \\ \frac{1}{\rho}\frac{\partial p}{\partial x} \\ 0 \\ 0 \end{pmatrix}, G_a = \begin{pmatrix} v \\ 0 \\ \frac{1}{\rho}\frac{\partial p}{\partial y} \\ 0 \end{pmatrix}, H_a = \begin{pmatrix} w \\ 0 \\ 0 \\ \frac{1}{\rho}\frac{\partial p}{\partial z} \end{pmatrix}. \quad (5)$$

with $Q = (0,\ 0,\ 0,\ -g\ )^T$. $(u,\ v,\ w)$ are the components of the velocity in the $x-$, $y-$ and $z-$directions, respectively, p is the total pressure, and g is the gravitational acceleration. $\nu_e = \nu + \nu_t$ is the effective viscous coefficient, in which ν is the kinematic viscosity and ν_t is the eddy viscosity to be determined with a turbulence model. The local density ρ and viscosity ν_e are given as in terms of α

$$\rho = \alpha\rho_w + (1-\alpha)\,\rho_a,\ \ \nu_e = \alpha\nu_{\not e} \ \ + (1-\alpha)\,\nu_{ae} \quad (6)$$

where the subscripts (w, a) denote the water and air, respectively.

An Implicit Cell-Staggered Finite Volume Method

In this solver, we use a staggered grid arrangement: the pressure and α are located at the center of a cell, while three components of the velocity lie in the center of the corresponding cell face. With an implicit FV method, the discretization of the integral form of the conservation of Eq. (2) over each cell is written by

$$\left(\frac{\partial\varphi}{\partial t}\right)^{n+1} + \frac{1}{V}\sum_{faces}\overline{F}^{n+1} = Q^{n+1} \quad (7)$$

for an arbitrary fixed volume V with a cell face S. $\overline{F} = (Fn_x + Gn_y + Hn_z)S$. The subscript, $faces$, presents the summation over all cell faces surrounding a hexahedral cell. $(n_x,\ n_y,\ n_z)$ are the unit normal components of the cell face outwards in the $x-, y-$ and $z-$directions, respectively.

An implicit approach is thought to be more efficient in studying slowly transient flow, due to in principle without restriction of time step. However, since a large coupled set of non-linear equations has to be solved at each time step, an approximation for Eq. (7) is reasonable, such as by enforcing a local linearization of the fluxes from the convective and diffusion terms. Namely

$$\overline{F}^{n+1} = \overline{F}^{n} + \frac{\partial\overline{F}}{\partial\varphi}\delta\,\varphi \quad (8)$$

where the Delta form $\delta\varphi = \varphi^{n+1} - \varphi^n$. This leads to Eq. (7) as

$$\delta\varphi + \frac{\Delta t}{V}\sum_{faces}\left(\frac{\partial\overline{F}}{\partial\varphi}\right)\delta\varphi = \Delta t R \quad (9)$$

with the residual R of the momentum equations defined as

$$R = -\left(\frac{1}{V}\sum_{faces}\overline{F}^{n} - Q^n\right) \quad (10)$$

where Δt is a local time step determined according to the CFL (Courant Friedrichs Lewy) constraint. $Q^{n+1} = Q^n$.

Evaluation of the Derivative $\frac{\partial\overline{F}}{\partial\varphi}$ We adopt the following two approximations for evaluation of the derivative $\frac{\partial\overline{F}}{\partial\varphi}$: one is to use an one-order upwind scheme for the convective fluxes; another is to neglect the cross derivatives associated with the viscid fluxes. For example, the convective fluxes in the $x-$momentum equation may be derived by

$$\frac{\partial uu}{\partial x} + \frac{\partial vu}{\partial y} + \frac{\partial wu}{\partial z} = \frac{1}{V}\sum_{faces} u_n u S = \frac{1}{V}\sum_{faces}\dot{M}u \quad (11)$$

where u_n is a normal face velocity defined as $u_n = un_x + vn_y + wn_z$, and $\dot{M} = u_n S$ is the volumetric fluxes across a certain face.

Thus, the derivative $\frac{\partial\overline{F}}{\partial u}$, such as at the right state of the cell face, $(i+\frac{1}{2})$, may be evaluated by

$$\left(\frac{\partial\overline{F}}{\partial u}\right)_{i+\frac{1}{2}} = \dot{M}_{i+\frac{1}{2}} \quad (12)$$

With an one-order upwind scheme, the convective fluxes on the face $(i+\frac{1}{2})$ are given as

$$\left(\dot{M}\delta\varphi\right)_{i+\frac{1}{2}} = \dot{M}^{+}_{i+\frac{1}{2}}\delta\varphi_i - \dot{M}^{-}_{i+\frac{1}{2}}\delta\varphi_{i+1} \quad (13)$$

in which $\dot{M}^{+}_{i+\frac{1}{2}}$ and $\dot{M}^{-}_{i+\frac{1}{2}}$ are formulated by

$$\dot{M}^{+}_{i+\frac{1}{2}} = max\left(\ \dot{M}_{i+\frac{1}{2}}, 0\right),\ \ \dot{M}^{-}_{i+\frac{1}{2}} = max\left(-\dot{M}_{i+\frac{1}{2}}, 0\right)$$

For the viscous fluxes, these read as

$$\nu_e\left(\frac{\partial^2\varphi}{\partial x^2} + \frac{\partial^2\varphi}{\partial y^2} + \frac{\partial^2\varphi}{\partial z^2}\right) = \frac{\nu_e}{V}\sum_{faces}\frac{\partial\varphi}{\partial n}S \quad (14)$$

where $\frac{\partial\varphi}{\partial n}$ is the normal gradient at a certain face defined by

$$\frac{\partial\varphi}{\partial n} = \frac{\partial\varphi}{\partial x}n_x + \frac{\partial\varphi}{\partial y}n_y + \frac{\partial\varphi}{\partial z}n_z$$

With a central difference scheme, one obtains

$$\begin{aligned}\left(\frac{\partial\overline{F}}{\partial u}\right)_{i+\frac{1}{2}}\delta\varphi \ &= \ \nu_e\frac{\partial}{\partial u}\left(\frac{\partial\varphi}{\partial n}S\right)_{i+\frac{1}{2}}\delta\varphi \\ &= \left(\delta u_{i+1} - \delta u_i\right)K_{i+\frac{1}{2}}\end{aligned} \quad (15)$$

where $K_{i+\frac{1}{2}} = \left(\frac{\nu_e S}{\Delta x}\right)_{i+\frac{1}{2}}$ is the volumetric viscous fluxes, Δx is the corresponding cell thickness. In this way, the bandwidth of the linear equation is kept as a set of tridiagonal block that may be resolved by the alternative directional implicit (ADI) approach.

Solution of the Delta Form $\delta\varphi$ Define $A_{(i\pm1)}$ are a blend of these two coefficients associated with the volumetric fluxes $(\dot{M})$ and viscous fluxes (K), i.e.,

$$A_{i+1} = \frac{\Delta t}{V}\left(K_{i+\frac{1}{2}} + \dot{M}^{-}_{i+\frac{1}{2}}\right),\ A_{i-1} = \frac{\Delta t}{V}\left(K_{i-\frac{1}{2}} + \dot{M}^{+}_{i-\frac{1}{2}}\right)$$

where the subscript $(i-\frac{1}{2})$ represents the left state of the cell face. With the ADI algorithm, Eq. (9) can be factored into three one-dimensional equations. Namely

$$\begin{aligned} A^{(1)}_p\delta\varphi^{**} - \ & A_{i+1}\delta\varphi^{**}_{i+1} - A_{i-1}\delta\varphi^{**}_{i-1} = \Delta t R \\ A^{(2)}_p\delta\varphi^{*} - & A_{j+1}\delta\varphi^{*}_{j+1} - A_{j-1}\delta\varphi^{*}_{j-1} = \delta\varphi^{**} \\ A^{(3)}_p\delta\varphi - & A_{k+1}\delta\varphi_{k+1} - A_{k-1}\delta\varphi_{k-1} = \delta\varphi^{*} \end{aligned} \quad (16)$$

in which the mainly diagonal coefficients $A_p^{(1)}, A_p^{(2)}$ and $A_p^{(3)}$ are

$$A_p^{(1)} = 1 + A_{i+1} + A_{i-1} + \frac{\Delta t}{V}\left(\dot{M}_{i+\frac{1}{2}} - \dot{M}_{i-\frac{1}{2}}\right)$$
$$A_p^{(2)} = 1 + A_{j+1} + A_{j-1} + \frac{\Delta t}{V}\left(\dot{M}_{j+\frac{1}{2}} - \dot{M}_{j-\frac{1}{2}}\right)$$
$$A_p^{(3)} = 1 + A_{k+1} + A_{k-1} + \frac{\Delta t}{V}\left(\dot{M}_{k+\frac{1}{2}} - \dot{M}_{k-\frac{1}{2}}\right)$$

(i, j, k) denote cell number in the $x-$, $y-$ and $z-$directions, respectively. $(i+1)$ and $(i-1)$ are two neighbours of cell i. Similar definition is for $A_{j\pm1}$ and $A_{k\pm1}$ by index substitution.

A Poisson Equation for the Pressure The temporal velocity $\tilde{\varphi} = \varphi^n + \delta\varphi$ is not, in general, divergence-free. According to the projected algorithm, it is used for updating the pressure so that the final velocity field satisfies the continuity equation. Thus, substituting the resulting velocity into the following continuity equation,

$$\sum_{faces} \left\{\left(un_x + vn_y + wn_z\right) S\right\}^{n+1} = 0 \tag{17}$$

one obtains

$$\sum_{faces} \left\{\frac{1}{\rho}\left(\frac{\partial p}{\partial n}\right) S\right\}^{n+1} = \frac{1}{\Delta t}\sum_{faces} \widetilde{u}_n \tag{18}$$

where $\frac{\partial p}{\partial n}$ is the normal face gradient at a certain face. With a central-difference scheme, Eq. (18) can be written as a Poisson-type equation for the pressure, which may be resolved by the direct solution methods like the ICCG (incomplete Cholessky conjugate gradient) algorithm or iterative methods like the SOR (successive over-relaxation) scheme.

Based on a quadratic backward approximation in time, an implicit three-level second-order scheme is implemented for time derivative,

$$\left(\frac{\partial \varphi}{\partial t}\right)^{n+1} = \frac{3\varphi^{n+1} - 4\varphi^n + \varphi^{n-1}}{2\Delta t} \tag{19}$$

where the superscripts $(n+1,\ n,\ n-1)$ stand for the next, current and previous time levels, respectively. Therefore, the resulting velocity at the $(n+1)$th time level is realized by

$$\varphi^{n+1} = \frac{2}{3}\left(\varphi^n - \frac{1}{2}\varphi^{n-1} + \tilde{\varphi} - \frac{\Delta t}{\rho}\frac{\partial p}{\partial x_i}\right) \tag{20}$$

provided that the pressure from the Poisson solver is available. $(x_i i\ = 1, 2, 3) = (x_1, x_2, x_3) = (x, y, z)$. During the iterative course, one under-relaxation technique is implemented for the final velocity.

Evaluation of the Explicit Fluxes At the nth time step, for example, the explicit inviscid fluxes, $\sum_{faces} \overline{F}^n$ (see Eq. 10), are evaluated with the flux-difference splitting approach, once the face value φ is given by

$$\varphi_{i+\frac{1}{2}} = \begin{cases} \varphi^R_{i+\frac{1}{2}}, & \text{if } u_n < 0 \\ \varphi^L_{i+\frac{1}{2}}. & \text{if } u_n \geq 0 \end{cases} \tag{21}$$

where $\varphi^L_{i+\frac{1}{2}}$ and $\varphi^R_{i+\frac{1}{2}}$ are the variable values of the left and right states at $(i+\frac{1}{2})$ face, respectively. These may be obtained with the MUSCL (monotone upstream-centered scheme for conservation laws) scheme or the ENO (essential nonoscillation) scheme (Sussman et al., 1994). For the latter approach, $\varphi^L_{i+\frac{1}{2}}$ and $\varphi^R_{i+\frac{1}{2}}$ are formulated as

$$\begin{aligned} \varphi^L_{i+\frac{1}{2}} &= \varphi_i + \frac{1}{2} m\left(\varphi_{i+1} - \varphi_i, \varphi_i - \varphi_{i-1}\right) \\ \varphi^R_{i+\frac{1}{2}} &= \varphi_{i+1} - \frac{1}{2} m\left(\varphi_{i+2} - \varphi_{i+1}, \varphi_{i+1} - \varphi_i\right) \end{aligned} \tag{22}$$

and the function $m\left(a, b\right)$ is defined as

$$m\left(a, b\right) = \begin{cases} a, & \text{if } \mid a \mid \leq \mid b \mid \\ b. & \text{otherwise} \end{cases}$$

In general, the MUSCL and the ENO schemes approximate the convective flux difference with a second-order accuracy in smooth region. In the vicinity of a cut cell and surface cell, an one-order upwind scheme is imposed instead of these two approches.

An Artificial Damping Term The normal face velocity u_n at a certain face is obtained by

$$\left(u_n\right)_{i+\frac{1}{2}} = \frac{1}{2}\left\{\left(u_n\right)_i + \left(u_n\right)_{i+1}\right\} \tag{23}$$

for evaluation of the volumetric flux $\dot{M}_{i+\frac{1}{2}}$ at $(i+\frac{1}{2})$ face. The linear interpolation of the face value is a second-order accuracy (with central differencing) but results in an unbounded solution for convective dominated problems. On the other hand, a high-order upwind scheme may lead to unphysical oscillations owing to its non-monotone behaviour, whereas its implementation can increase the accuracy of the results. For solution of such problems, one approach is to introduce artificial dissipation terms that may remove high frequence oscillations. As a result, numerical stability can be enhanced. In this way, we define

$$\left(u_n^*\right)_{i+\frac{1}{2}} = \left(u_n\right)_{i+\frac{1}{2}} - d_{i+\frac{1}{2}} \tag{24}$$

where $d_{i+\frac{1}{2}}$ is the second- and fourth-order artificial damping terms, respectively. It can be expressed as the following compact form in terms of variables of the right (R) and left (L) sides at a certain face:

$$d_{i+\frac{1}{2}} = \frac{1}{2\rho\psi_2 c_2}\left(p^R_{i+\frac{1}{2}} - p^L_{i+\frac{1}{2}}\right)_1 - \frac{1}{2\rho\psi_4 c_4}\left(p^R_{i+\frac{1}{2}} - p^L_{i+\frac{1}{2}}\right)_3 \tag{25}$$

where the subscripts $(1,\ 3)$ imply that an one-order upwind scheme and third-order upwind scheme are implemented for evaluation of variables at the left and right, respectively. c_2 and c_4 are coefficients, and ψ_2 orψ_4 is of the same order as the flow field velocity. Note that first- and third-derivative terms in the pressure (see Eq. 25) add numerical dissipations similar to those created by the second- and fourth-order dissipation terms. They become negligible with smooth pressure fields but suppress the oscillatory behavior in the region of strong pressure gradient, because of their high-frequency damping capability.

Operator Split Advection Algorithm for α

According to the relation with neighboring cells, an interface over each surface cell is reconstructed either horizontally or vertically at each time step, which is directly borrowed the basic idea from Hirt-Nichols's algorithm. Thus, with an operator split advection algorithm, the following equation is resolved within a whole computational domain in each spatial direction instead of Eq. (1):

$$\frac{\partial \alpha}{\partial t} + \frac{\partial (u\alpha)}{\partial x} + \frac{\partial (v\alpha)}{\partial y} + \frac{\partial (w\alpha)}{\partial z} = \alpha \left\{ \frac{\partial u}{\partial x} + \frac{\partial v}{\partial y} + \frac{\partial w}{\partial z} \right\} \quad (26)$$

Using a FV approach, this may be discretized as

$$\frac{\alpha^{n+1} - \alpha^n}{\Delta t} = -\frac{1}{V} \sum_{faces} \left(\dot{M} \alpha \right) + \frac{\alpha}{V} \sum_{faces} \left(\dot{M} \right) \quad (27)$$

Furthermore, Eq. (27) is split as

$$\begin{aligned} \alpha^* &= \alpha^n - \frac{\Delta t}{V} \alpha^{(1)} \\ \widetilde{\alpha} &= \alpha^* - \frac{\Delta t}{V} \alpha^{(2)} \\ \alpha^{n+1} &= \widetilde{\alpha} - \frac{\Delta t}{V} \alpha^{(3)} \end{aligned} \quad (28)$$

in which $\alpha^{(1)}, \alpha^{(2)}$ and $\alpha^{(3)}$ denote as

$$\begin{aligned} \alpha^{(1)} &= \left(\dot{M} \alpha^n \right)_{i+\frac{1}{2}} - \left(\dot{M} \alpha^n \right)_{i-\frac{1}{2}} + \alpha^n \left(\dot{M}_{i+\frac{1}{2}} - \dot{M}_{i-\frac{1}{2}} \right) \\ \alpha^{(2)} &= \left(\dot{M} \alpha^* \right)_{j+\frac{1}{2}} - \left(\dot{M} \alpha^* \right)_{j-\frac{1}{2}} + \alpha^* \left(\dot{M}_{j+\frac{1}{2}} - \dot{M}_{j-\frac{1}{2}} \right) \\ \alpha^{(3)} &= \left(\dot{M} \widetilde{\alpha} \right)_{k+\frac{1}{2}} - \left(\dot{M} \widetilde{\alpha} \right)_{k-\frac{1}{2}} + \widetilde{\alpha} \left(\dot{M}_{k+\frac{1}{2}} - \dot{M}_{k-\frac{1}{2}} \right) \end{aligned}$$

where α^* and $\widetilde{\alpha}$ represent the corresponding values of α at the end of each sweeping fractional step, respectively. This involves the sweep in the $x-$direction for updating α^*, and then followed the sweeps in $y-$ and $z-$directions, respectively, for updating $\widetilde{\alpha}$ and α^{n+1}. Indices, $(j \pm \frac{1}{2})$ and $(k \pm \frac{1}{2})$, stand for the corresponding cell face in the $y-$ and $z-$directions, respectively. To avoid the introduction of system error, their order is inverted. With this Eulerian interface reconstruction, a volume flux at a certain face, such as $\dot{M}_{i+\frac{1}{2}} = (u_n S)_{i+\frac{1}{2}}$, is always available. An essential point is how to evaluate the volume fraction $\alpha_{i+\frac{1}{2}}$ at the corresponding face in case the sharpness and shape of the interface are maintained. To achieve this, Ubbink and Issa's high resolution method is implemented, including a second-order explicit Adams-Bashforth formulation for the time integration.

This procedure can be made second-order simply by alternating the sweep direction at each time step. In other words, this approach is simple and effective because it can maintain the front sharp and provide such desirable properties during tracking interface.

A Cut-Cell Cartesian Technology

Since the resulting matrix equation is solved with the tridiagonal matrix algorithm (TDMA) for the delta form and the ICCG algorithm for the pressure, they must be applied to the whole computational domain. This is regardless of whether a cell represents fluid, surface, void, or an obstacle that involves with or without a cut boundary. It is no problem to find the solution over a fluid or surface cell. However, singularities occur in void and whole obstacle cells, where ρ is zero for the former and undefined for the latter. One approach for this problem is to add a considerable value to the mainly diagonal coefficients in the linear equation. Furthermore, over a cut cell, the effect of a sturcture is also incorperated through introduction of an effective geometry space covered a fluid. Note that void and whole obstacle cells are internal Dirichlet and Neumann boundaries, respectively. They may be realized in the operator matrix by manipulating the corresponding elements. Additionally, arbitrarily small cut cells are treated carefully, expecially when a mesh is refined. In this way, the pressure over this cell is extrapolated linearly, because it is placed at the center of a cell. But the velocity does not handled due to its staggered arrangement related with the pressure.

Initial and Boundary Conditions

Initial Conditions At $t = 0$, the water is at rest and the volume fraction α is initially assigned according to the still water level. The hydrostatic pressure is used as initial state for the pressure.

Boundary Conditions For the pressure, it is not necessary to specify the boundary conditions with the ICCG algorithm, except at the free surface. The wall effect is incorporated by enforcing the slip boundary conditions for a cut cell or no-slip conditions for a mesh boundary. At the free surface, the simplified dynamic boundary conditions like a potential flow are imposed. This implies that the effects of a viscous and the surface tension are neglected. Owing to $p = 0$ at a free surface, the matrix at all surface

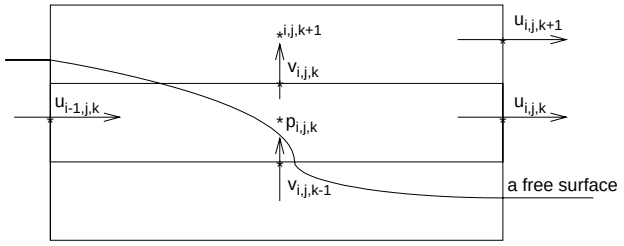

Figure 2: Implementation of the free-surface tangential dynamic boundary conditions.

cells is dealt with by setting the corresponding coefficient to zero. For the velocity over surface cells exposed to the air, for example, $u_{i\,j,k}$ cannot be renewed by the $x-$momentum equation (see Fig. 2). In such a case, it is enforced by the continuity equation, and $u_{i,j+1,k}$ is evaluated with the linear extrapolation. Furthermore, the pressure and α are evaluated with a mirror symmetry over a cut cell that contains both a free surface and a wall. At the inlet, a wave generator is located (Troch and Rouck, 2000), in which the incident waves are generated according to the linear wave theory. To reduce the generation of non-physical high-frequency waves, an adjustment function is implemented for the

wave height and the velocity at the inlet. It smoothly increase to unity from its initial value of zero. At the outlet, Orlanski's open boundary condition is applied to dissipate the energy of outgoing waves. It may be espressed as

$$\frac{\partial \beta}{\partial t} + c\frac{\partial \beta}{\partial x} = 0 \tag{29}$$

where $\beta = (u,\ v,\ w,\ \alpha)$. c is the phase velocity of the wave train and $c = \sqrt{gd}$ with a finite water depth d.

TEST CASES

Some test cases will be used for validation of our numerical method. First test case (in this paper, only one case is presented) is to simulate the breaking waves over a two-dimensional (2D) smooth impermeable sea dike without a turbulence model ($\nu_t = 0$ and $\nu_e = \nu = 1.3 \times 10^{-4}\ m^2$/s).

A Sea Dike

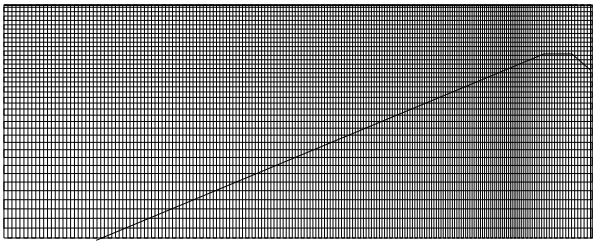

Figure 3: A Cartesian cut-cell mesh over a sea dike.

The geometry of the sea dike is shown in Fig. 1, where the seaward slope is 1:6, the landward slope is 1:3 and the crest height h is 0.8 m, including $l_1 = 1.0$ m, $s = 0.3$ m and $l_3 = 0.5$ m. With trivial effort, a Cartesian cut-cell mesh is generated (see Fig. 3), in which a typical computational domain consists of the total length 6.3 m and height 1 m. In the present case, cut cells always exist due to the use of a Cartesian grid (see Fig. 3), while the dike with a slope is described with a biquadratic function. These may be treated by predefining cells that may be fully or partially dry, in which the former (called a whole obstacle or internal obstacle cell) is characterized as zero velocity. For a regular wave at the inlet, the wave characteristics, such as the amplitude, period and wavelength together with the water depth, are given in Table 1.

Table 1: The wave height H, period T, wavelength λ and the water depth d.

$H\ (m)$	$T\ (s)$	$\lambda\ (m)$	$d\ (m)$
0.16	2.0	4.62	0.7

Calculated Results and Discussions

Convergence The iterative convergence is assessed by examining the L_2 norm of the residuals for the momentum equations and the pressure. For example, the residual for the $x-$momentum lies mostly between $10^{-2} \sim 10^{-3}$ in this case.

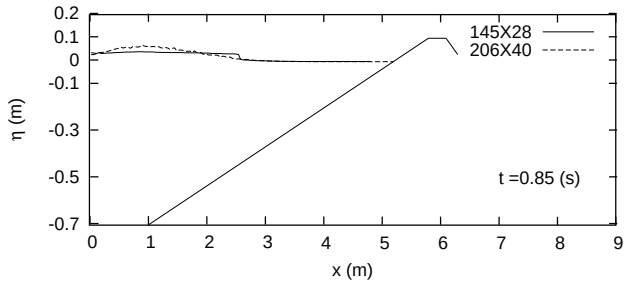

Figure 4: Surface elevations with two different grids. t =0.85 s.

Grid Effects Fig. 4 displays the effects of the grid density on the surface elevations η (m) along the $x-$direction (m). Two different grids with a refinement ratio of $\sqrt{2}$ are implemented, in which the coarse grid with varying cell sizes is 145×28 along the $x-$ and $z-$directions, respectively, and the fine grid is 206×40. In this case, each grid approximates one or five days of the CPU time, dependent on the specified running time. It is observed that difference between them is obvious. With the coarse grid, the free surface is not sharply defined, while the fine mesh captures more detailed characteristic of motions. This implies that the physical phenomena of motions may be described well with the present fine grid (we tried a more fine mesh 290×56, but it needs more CPU time whereas the result is fine). Of course, local grid refinement is also attractive for improvement of accuracy over each surface cell. Note that during a relatively short time (in here, $t = 0.85$ s), this indicates that there is not significant reflection from a dike or appearance of reflection is little. Therefore, it is thought that the discrepancy of the results almost arises from the different grid density.

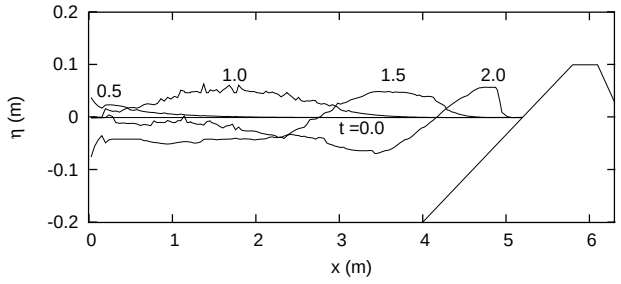

Figure 5: Development of waves with one period from initial stage.

Time Histories of Wave Development We represent a time history of the evolution of the interface at one initial period (see Fig. 5). Our computation starts with a flat free surface at t=0. The waves propagate towards a dike from t=0.5 s, and a big wave is generated at t=1.0 s. Finally, one can see the development of the expected wave motions, even on this relatively coarse grid (206×40).

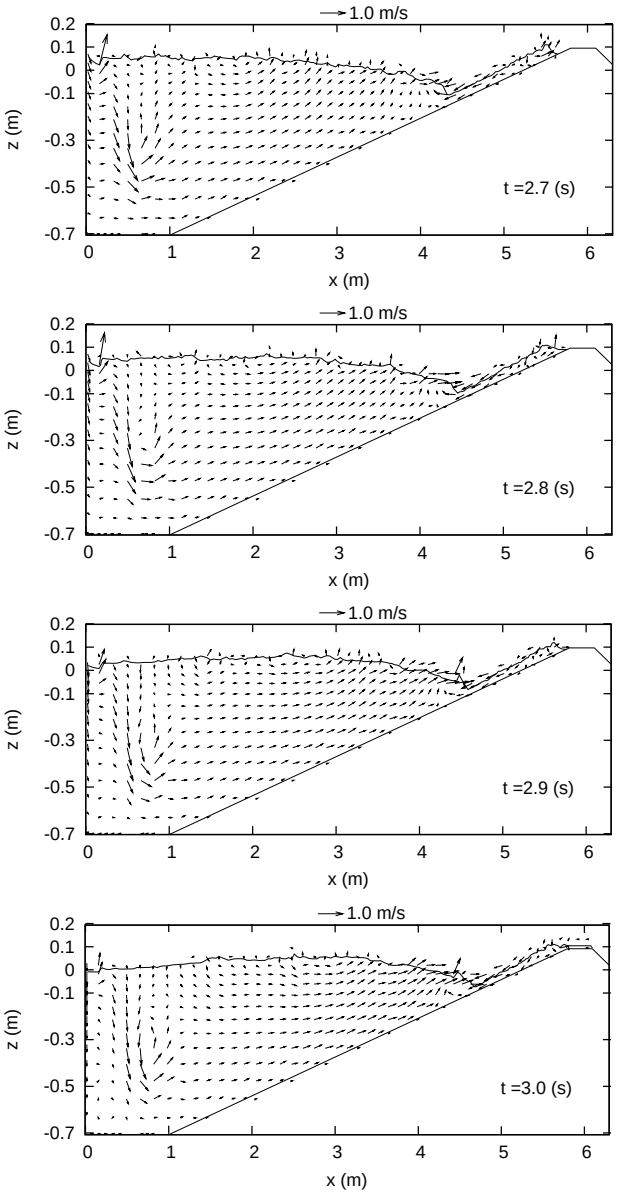

Figure 6: Process of an initial overtopping.

An Initial Overtopping Fig. 6 displays the generation of an initial overtopping during $t = 2.7$ to 3.0 s. It is understood that this is related with several stages like the wave attack, runup, rundown and overtopping, including breaking waves, as shown in Fig. 6.

Velocity Fields Fig. 7 illustrates the velocity fields at different time levels. During more waves, the features of the flow become

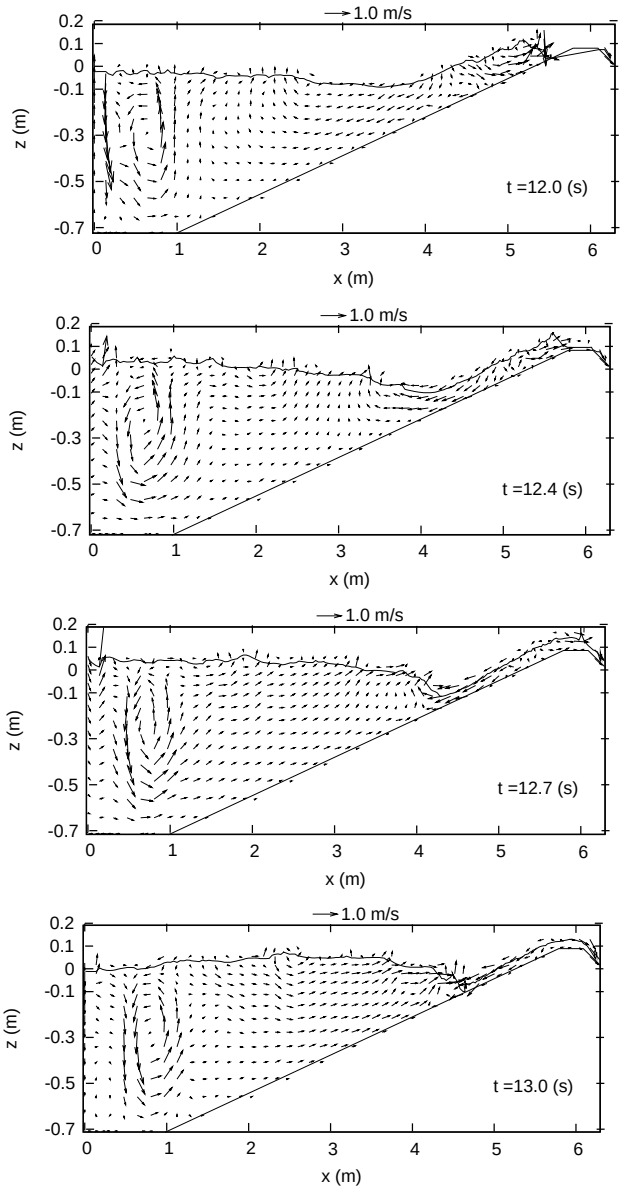

Figure 7: Velocity fields between t =12.0 and 13.0 (s).

very complex, which is related with shocks and vortices. It is observed that the steepness of a free surface is most likely associated with a cycle of splashing and the vortex formation created by the velocity. The roller-type vortices are generated by the breakup of the front of a wave or the reflection or both. The waves continuously break and a strong backflow is visible. These lead to the free surface to be deformed significantly, such as at $t = 13.0$ s (see Fig. 7). The energy may be dissipated by an artificial damping or turbulence and convected by vortices. At $t = 12.0$ s, a wave grows up significantly near $x = 5.0$ m. This indicates that an overtopping event will start again. As it propagates towards the crest of the dike, the peak of waves inclines gradually forward at $t = 12.4$ s, until it overtops this dike at $t = 12.7$ s (this is observed during the measurements). Finally, the motions at $t = 13.0$ s recover the stage at $t = 11.0$ s. Therefore, our solver captures the major

features of the flow: the formation of breaking waves. In particular, when the interface undergoes severe topological changes, the velocity and the pressure interact strongly each other.

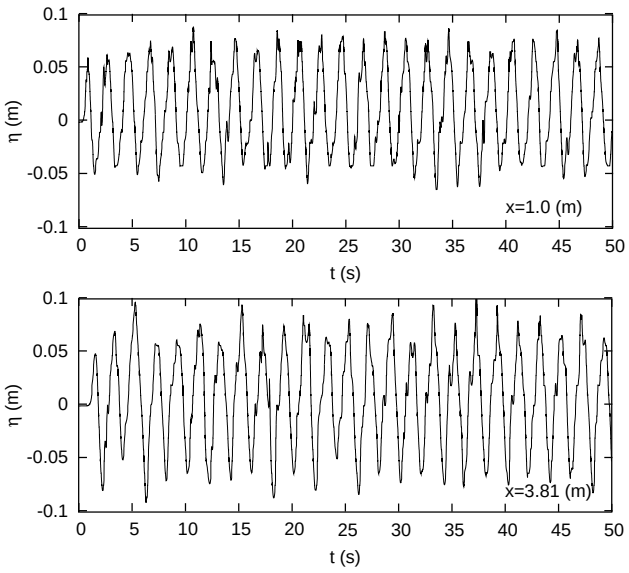

Figure 8: Time sequence of wave heights at two locations, x =1.0 and 3.81 (m).

Development of Waves at two Probes Time sequence of the wave heights at two locations of interest is shown in Fig. 8. The running time is $t = 25$ T and two wave probes are located at $x = 1.0$ and 3.81 m from the wavemaker, respectively. It is seen that the wave trains rapidly develop. The wave profile maintains a regular shape that exhibits typical non-linear features, in which the peak looks higher and narrower while troughs display smaller and flatter.

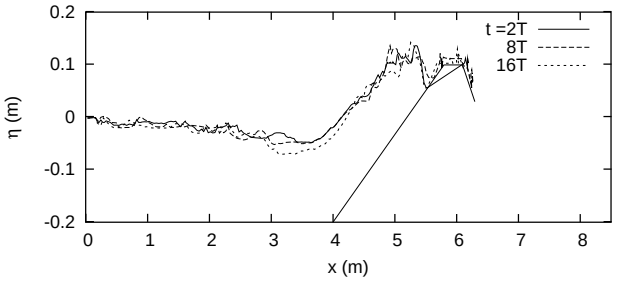

Figure 9: Comparison of wave profiles at $t = 2T$, $8T$ and $16T$.

Comparison of Wave Profiles at Three Different Time Levels We compare the wave profiles at three different time levels (see Fig. 9). First one is a short running time $t = 2$T, second is a relatively long time $t = 8$T and final is $t = 16$T. As expected, the result is satisfactory in the most regions and the difference of the phase is rather small. The location of breaking waves may be predicted well for all. This demonstrates that our computation is stable. Probably, one reason of the difference stems from the loss of the fluid volume due to the current overtopping.

CONCLUSIONS

We present a cell-staggered implicit VOF finite volume solver. The two essential features in our solver are the ability to capture a breaking wave over a cut-cell Cartesian mesh, and a computationally efficient algorithm for the coupling of the pressure and the velocity. The convergence property, the study of grid density and stability analysis are investigated (the calculated results will be compared with the experimental data in the next stage). This demonstrate our solver to work well. Overall, it can yield detailed flow information for the seadike design.

ACKNOWLEDGMENTS

The present work is carried out partly within the EU funded research project CLASH (EVK3-CT-2001-58), and partly within the research project G.0228.02 funded by the Fund for Scientific Research - Flanders (Belgium).

REFERENCES

Gueyffier, D., Li, J., Nadim, A., Scardovelli, R. and Zaleski, S (1999). "Volume-of-Fluid Interface Tracking with Smoothed Surfaces Stress Methods for Three-Dimensional Flows," $J.Comp.Phys.$, Vol 152, pp 423-456.

Hirt, C.W. and Nichols, B. D (1981). "Volume of Fluid Method for the Dynamics of Free Boundaries," $J.Comp.Phys.$, Vol 39, pp 201-225.

Lafaurie, B., Nardone, C., Scardovelli, R., Zaleski, S. and Zanetti, G (1994). "Modelling Merging and Fragmentation in Multiphase Flows with SURFER," $J.Comp.Phys.$, Vol 113, pp 134-147.

Li Tingqiu, Troch, P. and De Rouck, J (2003). "A Solver for Numerical Simulation of Breaking Waves Using a Cut-Cell VOF Cell-Staggered Finite-Volume Approach," Report, Department of Civil Engineering, Ghent University, Belgium.

Rider, W. J. and Kothe, D. B (1998). "Reconstructing Volume Tracking," $J.Comp.Phys.$, Vol 141, pp 112.

Sussman, M., Smereka, P. and Osher, S (1994). "A Level Set Approach for Computing Solutions to Incompressible Two-Phase Flow," $J.Comp.Phys.$, Vol 114, pp 146-159.

Troch, P. and De Rouck, J (1999). "An Active Wave Generate-Absorbing Boundary Condition for VOF Type Numerical Model," $Coastal\ Engineering$, Vol 38, pp. 223-247.

Ubbink, O. and Issa, R. I (1999). "A Method for Capturing Sharp Fluid Interfaces on Arbitrary Meshes," $J.Comp.Phys.$, Vol 153, pp 26-50.

Youngs, D. L (1982). "Time-Dependent Multi-Material Flow with Large Fluid Distortion," In Numerical Methods for Fluid Dynamics, ed. Morton, K. W. and Baines, M. J.